Spin-Flop Coupling and Exchange Bias in Embedded Complex Oxide Micromagnets

Yayoi Takamura,[1,*] Erik Folven,[2] Jonathan B. R. Shu,[1] Karl R. Lukes,[1] Binzhi Li,[1] Andreas Scholl,[3]
Anthony T. Young,[3] Scott T. Retterer,[4] Thomas Tybell,[2] and Jostein K. Grepstad[2]

[1]*Department of Chemical Engineering and Materials Science, University of California, Davis, Davis, California 95616, USA*
[2]*Department of Electronics and Telecommunications, Norwegian University of Science and Technology, NO-7491 Trondheim, Norway*
[3]*Advanced Light Source, Lawrence Berkeley National Laboratory, Berkeley, California 94720, USA*
[4]*Center for Nanophase Materials Sciences, Oak Ridge National Laboratory, Oak Ridge, Tennessee 37831, USA*
(Received 26 June 2013; published 3 September 2013)

The magnetic domains of embedded micromagnets with $2~\mu\text{m} \times 2~\mu\text{m}$ dimensions defined in epitaxial $La_{0.7}Sr_{0.3}MnO_3$ (LSMO) thin films and $LaFeO_3$/LSMO bilayers were investigated using soft x-ray magnetic microscopy. Square micromagnets aligned with their edges parallel to the easy axes of LSMO provide an ideal experimental geometry for probing the influence of interface exchange coupling on the magnetic domain patterns. The observation of unique domain patterns not reported for ferromagnetic metal microstructures, namely divergent antiferromagnetic vortex domains and ''Z''-type domains, suggests the simultaneous presence of spin-flop coupling and local exchange bias in this system.

The control of magnetic properties of patterned thin films and heterostructures is crucial to their implementation in magnetoelectronic devices. Reduced dimensionality and confined geometry of micro- or nanostructures lead to domain states with intriguing properties for spintronic device engineering. Two examples include the curling vortex and flux–closure Landau states reported for ferromagnetic (FM) metal [1,2] and perovskite oxide [3] films patterned to submicron dimensions. For FM materials, these domain states are readily explained by a reduction in total energy by elimination of the magnetostatic energy at the expense of magnetocrystalline anisotropy and domain wall energies. Exchange coupled systems involving antiferromagnetic (AFM)/FM interfaces exhibit magnetic properties that differ from bulk materials, e.g., increased coercivity and exchange bias [4]. Recently, correlated AFM and FM vortex states, including a unique divergent AFM vortex state, were observed by Wu *et al.* [5] in single-crystalline NiO/Fe and CoO/Fe discs on Ag(001) substrates. The impact of nanostructuring on domain formation and exchange coupling in AFM/FM bilayers has primarily been studied in metallic systems [6–12] and remains largely unknown in perovskite oxides.

In many exchange coupled systems, the local AFM/FM domain structure and presence of uncompensated spins at the AFM interface play a crucial role [11,13–16]. The (001)-oriented interface between a *G*-type antiferromagnet and a ferromagnet is fully compensated and therefore is characterized by an equal number of positive and negative exchange interactions. Theoretical analysis by Finazzi and Koon [17,18] predicts that spin-flop coupling occurs, characterized by a uniaxial anisotropy of AFM spins perpendicular to the magnetization of the FM film [17–20], with no horizontal shift of the hysteresis loop (i.e., no exchange bias). For a *G*-type antiferromagnet with an orthorhombic

perovskite structure [e.g., $LaFeO_3$ (LFO)], it is predicted that the tilting of FeO_6 octahedra leads to staggered Dzyaloshinshkii-Moriya interactions between nearest neighbors, providing a bias field and exchange bias [21,22]. In experimental studies, x-ray photoemission electron microscopy (X-PEEM) was utilized to observe spin-flop coupling in AFM/FM $La_{0.7}Sr_{0.3}FeO_3$ (LSFO)/ $La_{0.7}Sr_{0.3}MnO_3$ (LSMO) superlattices [23]. In this case, each AFM domain was directly correlated to two types of smaller FM domains, both of which satisfied the perpendicular orientation between the AFM spins and the magnetization of the FM layer. The locations of these domains changed in a correlated fashion with increasing temperature. These findings indicate that the strength of the spin-flop coupling overcame the anisotropy of the LSFO layer and the pinning effect of structural domains which typically define AFM domains in thicker layers. However, it was not clear whether the AFM or FM domains determine the shape and location of the coupled domain structure.

In this Letter, we utilize X-PEEM to image the coupled AFM and FM domain patterns in LFO/LSMO bilayers. Bulk LFO possesses a high Néel temperature (T_N) ∼ 740 K with the AFM Néel vector oriented along the orthorhombic *a* axis [24,25]. In thin films, the anisotropy decreases with decreasing film thickness with a distribution of domains with their AFM spin axes oriented along in-plane $\langle 100 \rangle$ and $\langle 110 \rangle$ pseudocubic directions [26]. LSMO is a soft FM material with strong magnetocrystalline anisotropy with easy axes oriented along in-plane $\langle 110 \rangle$ directions in films under tensile strain [27]. The Curie temperature, T_C, of the LSMO layer was ∼270 K determined using a superconducting quantum interference device magnetometer. While this system with $T_C < T_N$ is fairly unusual in exchange bias studies, Cai *et al.* [28] have shown that exchange coupling occurs in FM/AFM systems,

regardless of the relative values of T_C and T_N. Both unpatterned regions and $2 \mu m \times 2 \mu m$ square platelets were investigated. At these dimensions, the structures lie at the boundary of the expected transition from flux closure to more complicated multidomain states [29]. An all perovskite oxide structure ensures an ideal model system consisting of epitaxial layers without uncompensated spins at the AFM/FM interface. A thickness of 10 unit cells (u.c.) is sufficient to preserve the AFM properties of the LFO epilayer and permits characterization by X-PEEM of both the AFM and FM layers. Differing B-site elements in the ABO_3 perovskite unit cell (Fe vs Mn) enables separate probing of the magnetic properties of each layer.

The LFO (10 u.c.)/LSMO (90 u.c.) bilayers were grown by pulsed laser deposition on (001)-oriented Nb-doped (0.05 wt%) $SrTiO_3$ (Nb:STO) substrates using growth conditions reported elsewhere [26]. Unit cell intensity oscillations were observed throughout the growth using reflection high-energy electron diffraction. Atomic force microscopy showed a step-and-terrace structure with submonolayer surface roughness on individual terraces. X-ray diffraction showed distinct thickness fringes around the out-of-plane reflections and rocking curve widths comparable with that of the substrate (full width at half maximum ~0.02°), indicating films of high crystalline quality. Microstructures with their edges oriented along $\langle 110 \rangle$ substrate directions were defined using a patterning technique based on local modification of the structural and magnetic order by Ar^+ ion implantation through a Cr hard mask [3].

Domain images were obtained with high spatial resolution (~ 40 nm) and element specificity at 100 and 300 K using the PEEM-3 microscope at the Advanced Light Source. X-PEEM exploits x-ray magnetic linear/circular dichroism (XMLD/XMCD) at Fe/Mn $L_{2,3}$ absorption edges and uses a series of electron lenses to capture the emitted secondary electrons from the sample surface (5–10 nm escape depth) in order to probe the AFM/FM properties, respectively [30]. A schematic of the measurement geometry is shown in Fig. 1(a). The x rays were incident upon the sample at a 30° angle with respect to the sample surface. The XMLD-PEEM images were recorded at photon energies of 720.9 and 722.7 eV, corresponding to A and B multiplets of the Fe L_2 absorption edge, where the XMLD effect for LFO is maximized with opposite sign [31]. The final domain images were calculated as the B/A intensity ratio for each pixel to eliminate any chemical and topographical contrast while enhancing the magnetic contrast. The x-ray polarization vector, E, was varied continuously from s to p polarization, i.e., from parallel to 60° inclination with the sample surface. The polarization angle ω was defined as 0° (90°) for p (s) polarization, respectively. Such polarization scans enable determination of the direction of the AFM spin axis using the equation for the XMLD intensity,
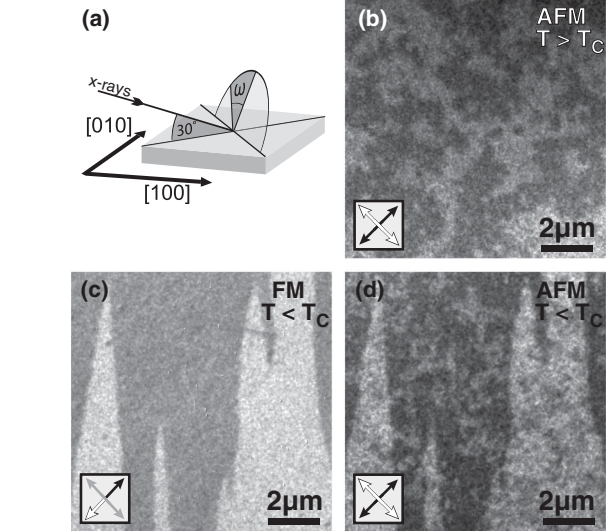

FIG. 1.   (a) X-PEEM measurement geometry; X-PEEM images showing (b) AFM domain structure at $T > T_C$ ($T = 300$ K), (c) FM domain structure at $T < T_C$ ($T = 100$ K), and (d) corresponding AFM domain structure for an unpatterned region of the LFO/LSMO bilayer. The legend in the lower left insets (b)–(d) illustrates the AFM or FM spin orientations associated with each contrast value. Fe XMLD-PEEM images were taken with $\omega = 90°$.

$I_{XMLD} = a + b(3\cos^2\theta - 1)\langle M^2 \rangle_T$, where a and b are constants, θ is the angle between E and the AFM spin axis, and $\langle M^2 \rangle_T$ is the temperature-dependent average of the magnetic moment squared. The maximum bright (dark) contrast corresponds to AFM domains with the AFM spin axis oriented parallel (perpendicular) to the x-ray E vector. XMCD-PEEM images were recorded with right and left circularly polarized (rcp and lcp) x-rays at a photon energy of 642.6 eV, corresponding to the maximum XMCD at the Mn L_3 edge for LSMO. The final domain images were obtained from the ratio of rcp/lcp images, such that bright, dark, and gray contrast corresponds to domains with antiparallel, parallel, and perpendicular orientation of the magnetization and the incident x rays, respectively. No XMCD was observed at the Fe L_3 edge, indicating that no uncompensated Fe moments are present near the LFO/LSMO interface. The XMCD-PEEM images were compared to FM domains simulated using the Object Oriented MicroMagnetic Framework (OOMMF) package [32] based on the Landau-Lifshitz-Gilbert equation. Input parameters for LSMO were saturation magnetization, $M_s = 400 \times 10^3$ A/m, exchange stiffness, $A = 1.7 \times 10^{-12}$ J/m, biaxial anisotropy constant $K_1 = 1600$ J/m³, and cell size = 5 nm [33,34]. The results were robust with changes in these parameter values.

Figure 1 shows X-PEEM images for an unpatterned region acquired at $T \sim 300$ K [Fig. 1(b)] and $T \sim 100$ K [Figs. 1(c) and 1(d)], i.e., corresponding to temperatures above and below T_C for the LSMO layer, respectively.

The samples were zero-field cooled in a chamber shielded
from magnetic fields to ~1% of the Earth's magnetic field.
Figures 1(b) and 1(d) are Fe XMLD-PEEM images
recorded with $\omega = 90°$, and Fig. 1(c) is a Mn XMCD-
PEEM image. Above T_C, we obtain the characteristic AFM
domain structure of a single-layer LFO film with irregu-
larly shaped domains of dark, bright, and gray contrast
[Fig. 1(b)] [26,31,35]. Below T_C, the AFM domain struc-
ture changes [Fig. 1(d)] with a direct correlation between
AFM and FM domains. Regions which appear bright [or
dark, not seen in Fig. 1(c)] in the Mn XMCD-PEEM image
are also bright in the Fe XMLD-PEEM image, while
regions which appear gray in the Mn XMCD-PEEM
image, are dark in the Fe XMLD-PEEM image. Domain
sizes range from less than one micron to tens of microns.
The FM domain contrast shown in Fig. 1(c) resembles
that observed for single-layer LSMO films with gray and
bright "flame-shaped" domains with magnetization along
in-plane $\langle 110 \rangle$ substrate directions, i.e., the magnetic easy
axes [27].

The orientation of the AFM spin axis in each domain
was determined by examining the local XMLD contrast as
a function of polarization angle, ω, and fitting the observed
contrast to the I_{XMLD} equation [26]. From this analysis, we
assign white or black AFM domains to regions where the
Néel vector lies along $[\bar{1}10]$ and $[110]$ directions, respec-
tively. Analysis of the Mn XMCD contrast allows us to
assign the orientation of the FM magnetization in the
LSMO layer. The respective orientations of the AFM
spin axis and the FM moments are indicated with arrows
in the insets to Fig. 1. The correlated AFM and FM
domains are found to have a perpendicular orientation
between the local AFM spin axis and FM moments, con-
sistent with spin-flop coupling. Therefore, these results
suggest that the strength of the spin-flop coupling is suffi-
cient to cause a 90° rotation of the AFM spin axis as the
sample is cooled below T_C of the LSMO layer. It should
be noted that the larger AFM domains are speckled with
smaller (~ 300–400 nm) domains of gray contrast. The
gray domains correspond to a minority population of
AFM domains with their easy axis oriented along $\langle 100 \rangle$
substrate directions. This additional set of AFM spin axes
in LFO epilayers grown on LSMO was discussed in a
previous communication [26], where the relative popula-
tion of $\langle 110 \rangle$-oriented (61%) to $\langle 100 \rangle$-oriented (39%)
domains was found to remain constant irrespective of
temperature, indicating that only $\langle 110 \rangle$-oriented domains
exhibit spin-flop coupling, while $\langle 100 \rangle$-oriented domains
remain unchanged.

Patterning by *e*-beam lithography and Ar^+ ion implan-
tation to form embedded microstructures [3], depicted
schematically in Fig. 2(a), strongly affects the magnetic
domain structure, as seen from the X-PEEM images of
$2~\mu m \times 2~\mu m$ micromagnets patterned with edges along
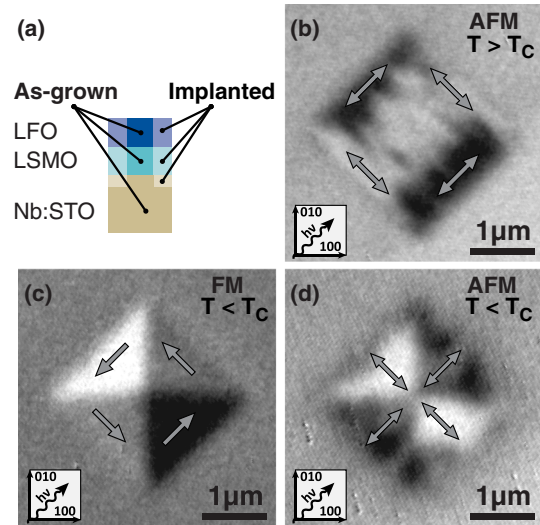in-plane $\langle 110 \rangle$ substrate directions, i.e., parallel to the

FIG. 2 (color online). (a) Cross section of embedded micro-
magnets in an implanted matrix. (b) AFM domain structure at
$T > T_C$ ($T = 300$ K) of $2~\mu m \times 2~\mu m$ bilayer micromagnets
oriented with edges parallel to $\langle 110 \rangle$ substrate directions; (c) FM
domain structure at $T < T_C$ ($T = 100$ K), and (d) corresponding
AFM domain structure. Arrows denote AFM or FM spin ori-
entations associated with each contrast value. Insets indicate the
experimental geometry.

magnetic easy directions of the LSMO layer. The image
in Fig. 2(b), recorded at $T > T_C$, shows the formation of
extended AFM domains with their Néel vector *parallel* to
the edges of the structures, as previously reported for this
system [26,36]. After zero field cooling to $T < T_C$, the Mn
XMCD-PEEM image [cf. Fig. 2(c)] unveils a flux-closure
domain structure with triangular domains of bright, dark,
and gray contrast for domains with magnetic moments
parallel, antiparallel, and perpendicular to the incident
x rays, respectively. The corresponding AFM domain con-
trast below T_C is shown in Fig. 2(d), where the AFM spin
axis orientation was determined from polarization angle
dependent XMLD-PEEM measurements and is indicated
with arrows. The AFM domains are consistent with spin-
flop coupling to the FM layer, with perpendicular orienta-
tion of the AFM spin axis and the FM moments. This
observation implies that the AFM spins are oriented *per-
pendicular* to the edges of the structure, consistent with the
divergent AFM vortex states reported by Wu *et al.* for NiO/
Fe and CoO/Fe discs [5], and requiring a 90° rotation
of the AFM spins compared to the configuration for
$T > T_C$. Figures 3(a) and 3(b) show FM and AFM domain
patterns, respectively, for an array of square micromagnets
patterned in the LFO/LSMO bilayer. Figure 3(c) shows the
FM domain patterns for a similarly structured single-layer
LSMO film, where the flux-closure domain pattern prevails
in 100% of the 23 square platelets imaged. In contrast, in
the bilayer micromagnets the formation of flux-closure
domain states is found only in 70% of the structures
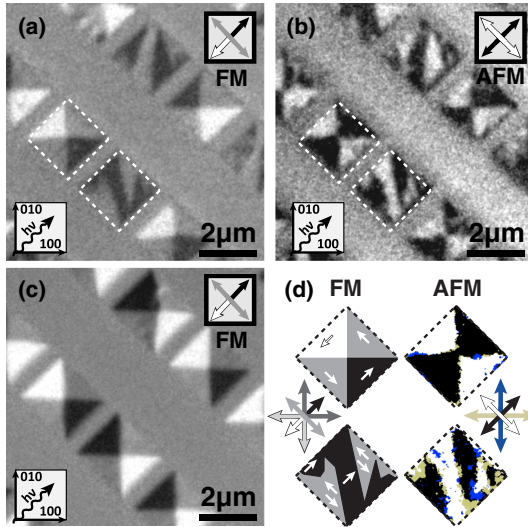(38 out of 55 micromagnets imaged). The remaining

FIG. 3 (color online). X-PEEM images of 2 μm $\times$ 2 μm micromagnets oriented with edges parallel to $\langle 110 \rangle$ substrate directions. (a) FM domain structure at $T < T_C$ ($T = 100$ K) and (b) corresponding AFM domain structure in the bilayer micromagnets. (c) FM domain structure at $T < T_C$ ($T = 100$ K) for a patterned single-layer LSMO film. (d) AFM domain maps deduced from polarization dependent measurements of micromagnets outlined in (b) and schematics of the FM domain structure deduced from micromagnets outlined in (a). Insets in the top right corner of (a)–(c) and in (d) show the mapping of image contrast to spin directions. Insets in the bottom left of (a)–(c) depict the experimental geometry.

30% of the bilayer micromagnets show a more complicated domain pattern resembling the letter "Z". Two variants of this Z-domain structure can be observed in Figs. 3(a) and 3(b). This domain structure has a net magnetic moment oriented 45° relative to the edges of the structure. Within the array of square micromagnets, the direction of this net magnetic moment appears to be randomly oriented between the four in-plane $\langle 100 \rangle$ directions. Analysis of the flux-closure domains in the bilayer micromagnets shows that their cores are displaced from the center of the square platelet by distances up to 175 nm, also leading to a net magnetic moment for individual structures. Again, we observe a direct correlation between the FM and AFM domains consistent with spin-flop coupling. A representative schematic of the two types of domain patterns is shown in Fig. 3(d).

In order to understand the formation of the FM domain structures in the 2 μm $\times$ 2 μm micromagnets, OOMMF simulations were carried out as shown in Fig. 4. With zero applied magnetic field ($\boldsymbol{H} = 0$ T), the 2 μm $\times$ 2 μm squares consistently show flux-closure domains, as seen in the single-layer LSMO [cf. Fig. 3(c)] and in 70% of the LFO/LSMO bilayer micromagnets. In order to explore the origin of the Z domains which exhibit a net magnetic moment [cf. Fig. 3(a)], $\boldsymbol{H}$ was applied 45° relative to the edges of the structures, i.e., along the [100] direction.
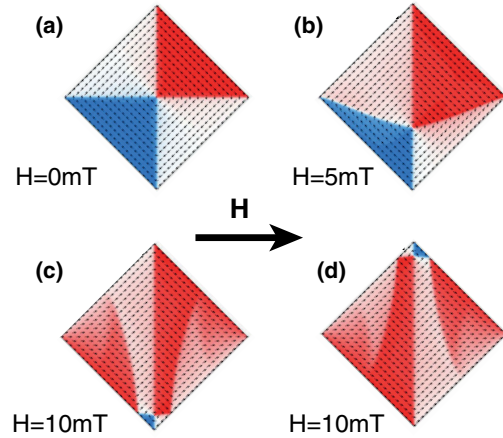

FIG. 4 (color online). OOMMF simulations for 2 μm $\times$ 2 μm micromagnets with edges parallel to $\langle 110 \rangle$ substrate directions and H applied along the [100] substrate direction. For $\boldsymbol{H} > 9$ mT, the domain pattern transitions from a flux-closure state with a shifted core to a Z domain. (c) and (d) Simulations reproducing the two variants of Z domains.

For small $\boldsymbol{H}$ values, the core of the flux-closure Landau pattern shifts from the center of the square, followed by a transition to a domain pattern resembling the experimentally recorded Z domains for fields above a threshold ~ 9 mT (Fig. 4). The OOMMF simulations reproduce the two variants of Z domains observed in the X-PEEM images. Because of the fact that the samples are shielded from externally applied magnetic fields in the PEEM-3 chamber and that the apparent local field is randomly distributed along in-plane $\langle 100 \rangle$ directions for individual micromagnets, this result suggests that the local magnetic field develops due to an exchange bias interaction between the LFO and LSMO layers. The random orientation of the exchange bias explains why no net shift of the bulk hysteresis loop was observed in blanket LSMO/LSFO superlattices [37]. At the same time, the spin-flop coupling at the LFO/LSMO interface remains robust enough to dictate a local perpendicular orientation of the AFM Néel vector and the FM magnetization, even in the presence of the exchange bias field. These unusual domain configurations observed in this all-perovskite oxide system can be explained by the absence of uncompensated spins at the (001) surface of the G-type antiferromagnet leading to spin-flop coupling, in concert with the tilting of FeO$_6$ octahedra in the orthorhombic unit cell leading to exchange bias.

In summary, we have investigated the coupled AFM and FM domain structures in 2 μm $\times$ 2 μm micromagnets embedded in an epitaxial LFO/LSMO bilayer. At these dimensions, the micromagnets lie at the boundary between flux-closure and more complicated multidomain states. For micromagnets with their edges aligned along the magnetic easy axis of LSMO (i.e., in-plane $\langle 110 \rangle$ substrate directions), the tilting of the FeO$_6$ octahedra due to the

orthorhombic structure leads to an exchange bias field along in-plane ⟨100⟩ directions. For increasing values of exchange bias field, the FM domain state transforms from flux-closure to Z domains. In all cases, the compensated nature of the (001) surface of the G-type antiferromagnet leads to AFM domains which maintain a spin-flop coupling configuration with the Néel vector oriented perpendicular to the FM magnetization. We have shown that coupling to an adjacent AFM layer can stabilize FM domain configurations with a net magnetization, even with zero applied magnetic field. The present findings encourage further studies on exchange bias and domain engineering in micromagnetic structures, both key factors for spintronic devices relying on patterned magnetic elements, such as patterned media for data storage and magnetic logic.

---

*ytakamura@ucdavis.edu

[1] T. Shinjo, T. Okuno, R. Hassdorf, K. Shogeto, and T. Ono, Science **289**, 930 (2000).

[2] A. Wachowiak, J. Wiebe, M. Bode, O. Pietzsch, M. Morgenstern, and R. Wiesendanger Science **298**, 577 (2002).

[3] Y. Takamura, R. V. Chopdekar, A. Scholl, A. Doran, J. A. Liddle, B. Harteneck, and Y. Suzuki, Nano Lett. **6**, 1287 (2006).

[4] J. Nogues and I. K. Schuller, J. Magn. Magn. Mater. **192**, 203 (1999).

[5] J. Wu, D. Carlton, J. S. Park, Y. Meng, E. Arenholz, A. Doran, A. T. Young, A. Scholl, C. Hwang, H. W. Zhao, J. Bokor, and Z. Q. Qiu, Nat. Phys. **7**, 303 (2011).

[6] J. Nogues, J. Sort, V. Langlais, V. Skumryev, S. Surinach, J. S. Munoz, and M. D. Baro, Phys. Rep. **422**, 65 (2005).

[7] W. Jung, F. J. Castano, and C. A. Ross, Phys. Rev. Lett. **97**, 247209 (2006).

[8] V. Baltz, J. Sort, S. Landis, B. Rodmacq, and B. Dieny, Phys. Rev. Lett. **94**, 117201 (2005).

[9] J. Sort, A. Hoffman, S.-H. Chung, K. S. Buchanan, M. Grimsditch, M. D. Baro, B. Dieny, and J. Nogues, Phys. Rev. Lett. **95**, 067201 (2005).

[10] J. Eisenmenger, Z.-P. Li, W. A. A. Macedo, and I. K. Schuller, Phys. Rev. Lett. **94**, 057203 (2005).

[11] T. Eimuller, T. Kato, T. Mizuno, S. Tsunashima, C. Quitmann, T. Ramsvik, S. Iwata, and G. Schutz, Appl. Phys. Lett. **85**, 2310 (2004).

[12] S. Laureti, S. Y. Suck, H. Haas, E. Prestat, O. Bourgeois, and D. Givord, Phys. Rev. Lett. **108**, 077205 (2012).

[13] G. Salazar-Alvarez, J. J. Kavich, J. Sort, A. Mugarza, S. Stepanow, A. Potenza, H. Marchetto, S. S. Dhesi, V. Baltz, B. Dieny, A. Weber, L. J. Heyderman, J. Nogues, and P. Gambardella, Appl. Phys. Lett. **95**, 012510 (2009).

[14] J. Sort, K. S. Buchanan, V. Novosad, A. Hoffmann, G. Salazar-Alvarez, A. Bollero, M. D. Baro, B. Dieny, and J. Nogues, Phys. Rev. Lett. **97**, 067201 (2006).

[15] I. V. Roshchin, O. Petracic, R. Morales, Z.-P. Li, X. Batlle, and I. K. Schuller, Europhys. Lett. **71**, 297 (2005).

[16] S. Bruck, J. Sort, V. Baltz, S. Surinach, J. S. Munoz, B. Dieny, M. D. Baro, and J. Nogues, Adv. Mater. **17**, 2978 (2005).

[17] M. Finazzi, Phys. Rev. B **69**, 064405 (2004).

[18] N. C. Koon, Phys. Rev. Lett. **78**, 4865 (1997).

[19] T. C. Schulthess and W. H. Butler, Phys. Rev. Lett. **81**, 4516 (1998).

[20] M. D. Stiles and R. D. McMichael, Phys. Rev. B **59**, 3722 (1999).

[21] S. Dong, Q. Zhang, S. Yunoki, J.-M. Liu, and E. Dagotto, Phys. Rev. B **84**, 224437 (2011).

[22] S. Dong, K. Yamauchi, S. Yunoki, R. Yu, S. Liang, A. Moreo, J.-M. Liu, S. Picozzi, and E. Dagotto, Phys. Rev. Lett. **103**, 127201 (2009).

[23] F. Yang, N. Kemik, A. Scholl, A. Doran, A. T. Young, M. D. Biegalski, H. M. Christen, and Y. Takamura, Phys. Rev. B **83**, 014417 (2011).

[24] G. H. Jonker, Physica (Utrecht) **22**, 707 (1956).

[25] M. Eibschutz, S. Shtrikman, and D. Treves, Phys. Rev. **156**, 562 (1967).

[26] E. Folven, A. Scholl, A. T. Young, S. Retterer, J. E. Boschker, T. Tybell, Y. Takamura, and J. K. Grepstad, Phys. Rev. B **84**, 220410(R) (2011).

[27] L. M. Berndt, V. Balbarin, and Y. Suzuki, Appl. Phys. Lett. **77**, 2903 (2000).

[28] J. W. Cai, K. Liu, and C. L. Chien, Phys. Rev. B **60**, 72 (1999).

[29] L. J. Heyderman, S. Czekaj, F. Nolting, E. Muller, P. Fischer, P. Gasser, and L. Lopez-Diaz, J. Appl. Phys. **99**, 063904 (2006).

[30] S. Anders, H. A. Padmore, R. M. Duarte, T. Renner, T. Stammler, A. Scholl, M. R. Scheinfein, J. Stohr, L. Seve, and B. Sinkovic, Rev. Sci. Instrum. **70**, 3973 (1999).

[31] A. Scholl, J. Stohr, J. Luning, J. W. Seo, J. Fompeyrine, H. Siegwart, J.-P. Locquet, F. Nolting, S. Anders, E. E. Fullerton, M. R. Scheinfein, and H. A. Padmore, Science **287**, 1014 (2000).

[32] M. J. Donahue and D. G. Porter, *OOMMF User's Guide, Version 1.0* (National Technical Information Service, Alexandria, 1999).

[33] E. J. Kim, J. L. R. Watts, B. Harteneck, A. Scholl, A. T. Young, A. Doran, and Y. Suzuki, J. Appl. Phys. **109**, 07D712 (2011).

[34] T. Nagai, H. Yamada, M. Konoto, T. Arima, M. Kawasaki, K. Kimoto, Y. Matsui, and Y. Tokura, Phys. Rev. B **78**, 180414 (2008).

[35] S. Czekaj, F. Nolting, L. J. Heyderman, P. R. Willmott, and G. van der Laan, Phys. Rev. B **73**, 020401(R) (2006).

[36] E. Folven, T. Tybell, A. Scholl, A. T. Young, S. Retterer, Y. Takamura, and J. K. Grepstad, Nano Lett. **10**, 4578 (2010).

[37] Y. Takamura, F. Yang, N. Kemik, E. Arenholz, M. D. Biegalski, and H. M. Christen, Phys. Rev. B **80**, 180417 (R) (2009).